PERGAMON

Journal of Structural Geology 26 (2004) 247–258

JOURNAL OF STRUCTURAL GEOLOGY

www.elsevier.com/locate/jsg

Detailed analysis of acoustic emission activity during catastrophic fracture of faults in rock

Xinglin Lei[a,b,*], Koji Masuda[a], Osamu Nishizawa[c], Laurence Jouniaux[d], Liqiang Liu[b], Wentao Ma[b], Takashi Satoh[a], Kinichiro Kusunose[c]

[a]*Institute of Geoscience, GSJ/National Institute of Advanced Industrial Science and Technology (AIST), Higashi 1-1-1, Tsukuba, Ibaraki 305-8567, Japan*
[b]*Institute of Geology & Laboratory of Tectonophysics, China Seismological Bureau, Beijing, China*
[c]*Institute of Geo-Resource and Environment, GSJ/National Institute of Advanced Industrial Science and Technology (AIST), Higashi 1-1-1, Tsukuba, Ibaraki 305-8567, Japan*
[d]*Laboratoire de Geologie, Ecole Normale Superieure, France*

Abstract

The detailed time-space distribution of acoustic emission (AE) events during the catastrophic fracture of rock samples containing a pre-existing joint or potential fracture plane is obtained under triaxial compression using a high-speed 32-channel waveform recording system, and the results are discussed with respect to the prediction and characterization of catastrophic fault failure. AE activity is modeled quantitatively in terms of the seismic *b*-value of the magnitude–frequency relation, the self-excitation strength of the AE time series, and the fractal dimension of AE hypocenters. Consistent with previous studies on rock samples containing a fracture plane with several asperities, the present analyses reveal three long-term phases of AE activity associated with damage creation on heterogeneous faults, each clearly identifiable based on the above parameters. A long-term decreasing trend and short-term fluctuation of the *b*-value in the phase immediately preceding dynamic fracture are identified as characteristic features of the failure of heterogeneous faults. Based on the experimental results it is suggested that precursory anomalies related to earthquakes and other events associated with rock failure are strongly dependent on the heterogeneity of the fault or rock mass. A homogeneous fault or rock mass appears to fracture unpredictably without a consistent trend in precursory statistics, while inhomogeneous faults fracture with clear precursors related to the nature of the heterogeneity.

Keywords: Rock sample; Acoustic emission; Microcracking; Fault nucleation

1. Introduction

The study of damage formation in jointed or bulk rock under stress is a subject of widespread interest, with relevance to both artificial applications such as optimization of geothermal recovery, oil recovery, safe design of nuclear waste repositories, and rock bursts, and natural processes such as volcanism and seismology. For many reasons, it is important to be able to predict the time, location and intensity of potential rock fracture. Fracture development in stressed rock has been observed extensively in the laboratory by a number of methods. One approach is the direct observation of samples by scanning electron microscopy (SEM) (e.g. Zhao, 1998) or optical microscopy (e.g. Cox and Scholz, 1988). Another method involves monitoring the hypocenter distribution of acoustic emission (AE) events caused by microcracking activity (e.g. Lockner et al., 1991; Lei et al., 1992, 2000c). Direct observation is a useful technique for both brittle and ductile deformation, but is limited in that only the surface of the test specimen can be observed. In contrast, AE techniques provide an analysis of the microcracking activity inside the rock volume, but are insensitive to ductile deformation, which does produce appreciable AE activity. However, AE techniques have an important advantage over other techniques in that tests can be performed under confining pressure, which is very important in the simulation of underground conditions.

The recent development of high-speed multi-channel waveform recording technology has made it possible to monitor the hypocenters of AEs associated with spontaneously/unstably fracturing processes in stressed rock samples with high precision. Such a system is capable of recording AE waveforms in 32 channels at sampling rates of

* Corresponding author. Correspondence address: Institute of Geoscience, GSJ/National Institute of Advanced Industrial Science and Technology (AIST), Higashi 1-1-1, Tsukuba, Ibaraki 305-8567, Japan. Tel. +81-298-61-2468; fax: +81-298-61-3697.
E-mail address: xinglin-lei@aist.go.jp (X. Lei).

0191-8141/03/$ - see front matter © 2003 Elsevier Ltd. All rights reserved.
doi:10.1016/S0191-8141(03)00095-6

up to 5000 events per second, and have been successfully used to study the quasi-static nucleation of intact brittle rocks based on detailed AE data. The present authors applied this technique to the analysis of hornblende schist (Lei et al., 2000c) and granitic rocks (Lei et al., 2000a), and later to study of the fracture of mudstone containing quartz veins, which play a role as strong asperities (Lei et al., 2000b). More recently, the present authors observed that the microcracking activity associated with the fracture of an inhomogeneous fault proceeds in three stages with a spatial hierarchical structure (Lei et al., 2003).

The present report presents the experimental results for four samples with a naturally healed macroscopic joint and widely differing healing strength and asperity distributions. High-speed waveform recording technology was employed to monitor the detailed time–space distribution of AE activity during the catastrophic fracture of the four rock samples under triaxial compression. This report focuses on the experimental facts related to the temporal change of some quantitative statistics of AE activity, including the event rate, seismic *b*-value, self-excitation strength and fractal dimension of the hypocenter distribution.

2. Experiments and data analyses

2.1. Samples and experiments

Four samples having a macroscopic joint or potential fracture plane were prepared to simulate four kinds of faults of widely differing healing strength or asperity distribution. As all samples fractured along this pre-existing joint or potential fracture plane, the general term ‘fault’ is used to refer to that feature in this paper. For convenience, these samples are labeled SF (strong fault with homogeneous healing strength distribution), HF (fault with heterogeneous healing strength distribution), AF (fault with weak segments and strong asperities), and WF (weak fault with homogeneous strength distribution). The terms ‘strong’ and ‘weak’ are based on the fracture strength of the sample. As there is no way to know the detailed distribution of healing strength on the fault plane, the terms ‘homogeneous’ and ‘heterogeneous’ are mainly given in terms of optical microscope and naked eye observations, and as such are qualitative descriptions.

The host rock for the SF sample is a granitic porphyry, and is almost entirely free of microcracking (see Lei et al. (2000a) for reference). The main rock-forming minerals are quartz, plagioclase, and K-feldspar, with a grain size distribution of ~1 mm to ~1 cm (peak ~5 mm). As illustrated in Fig. 1a, no visible cracks can be seen by microscope observation along the fault in the SF sample. Therefore, the SF sample represents a strongly healed fault in a coarse-grained granitic porphyry.

The HF sample is a coarse-grained granite containing quartz, K-feldspar, biotite and muscovite hornblende

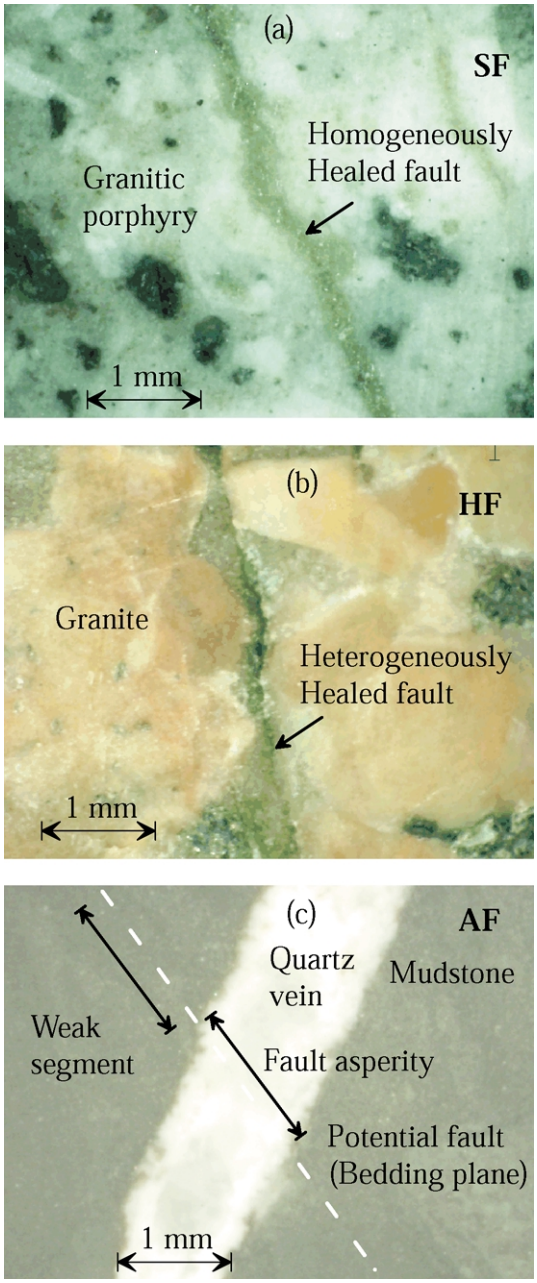

Fig. 1. Photomicrographs showing pre-existing or potential faults in the (a) SF, (b) HF and (c) AF samples.

(Jouniaux et al., 2001). This sample has a significantly higher density of pre-existing microcracks than the SF sample. In addition, there are also some heterogeneously distributed cracks along the fault plane, as shown in Fig. 1b. Thus, the HF sample models a heterogeneously healed fault in coarse-grained granite.

The WF sample is a mudstone with well-oriented planar structure. The final fracture plane was created along the bedding plane of the mudstone, at an angle of ~25° to the maximum stress axis of the sample. Since the bedding plane makes this sample significantly weaker than the SF and HF samples, the WF sample models a homogeneous weak fault

that may undergo ductile deformation under confining pressure.

The AF sample is similar to the WF sample but contains quartz veins at an angle of ~70° to the fracture plane (Fig. 1c). The quartz veins are either 1 or 3 mm thick, but are much stronger than the surrounding mudstone. Accordingly, the AF sample is a model of a weak fault with a few strong asperities or barriers.

All samples used in this study contain a potential fault oriented at an angle of 25 ~ 30° to the maximum stress direction. These potential faults were ruptured during triaxial compressive test, giving four typical models of shear faults with widely differing strength distributions.

All samples were obtained as cylinders of 100 mm in length and 50 mm in diameter. The aspect ratio of these samples (2:1) is smaller than the usual 2.5:1 used in many experiments. All samples were dried under normal room conditions for more than one month and then compressed under a constant stress-rate (0.04 ~ 0.1 MPa/s) loading and constant confining pressure of 60 MPa (40 MPa for the HF sample) at room temperature (~25 °C).

Friction between the sample ends and the end-pieces plays a role in constraining horizontal deformation around the ends of the samples. The end effects under these conditions for fine-grained samples are generally more important than for coarse-grained samples because the latter exhibit appreciable dilatancy prior to failure (Lei et al., 1992). In this study, the test samples contain a potential fault, which is weaker than the host rocks. Therefore, as the dilatancy in these host rocks will be several times smaller than in the case of homogeneous intact rock, end effects are not considered to be a serious problem in this study.

A total of 32 piezoelectric transducers (PZT) (5 mm in diameter, resonant frequency of 2 MHz) were mounted on the surface of each test sample and the two end caps to detect AE signal from microcracking events. A series of eight cross-type strain gauges (16 channels) were mounted on the surface of the test samples to measure local axial and circumferential strains. The local volumetric strain (ε_v) was calculated from the axial (ε_a) and circumferential (ε_c) strains according to the equation $\varepsilon_v = \varepsilon_a + 2\varepsilon_c$. The strain gauges were located on both the pre-existing fault and the host rock, and the 16 channels were sampled with a dynamic range of 16 bits and a maximum sampling frequency of 1 kHz.

As introduced by Lei et al. (2000c), the high-speed waveform recording system used in this study records the maximum amplitudes (dynamic range of 100 dB) in two channels and waveforms (sampling rate of 20 MHz, 12-bit resolution) in 32 channels. The waveform recorder has a discrete A/D converter and 16 MB memory buffers for each channel. The sampling length is set to 1024 words (50 μs) for each event, corresponding to a total waveform recording capacity of 8192 events. The mask time (minimum trigger interval) for waveform recording was ~200 μs, which is sufficient for recording the full tail of typical detectable AE signals (generally about 50–200 μs in length), ensuring no major event loss. The system records 32 (channels) × 2048 (sampling length in bytes) × 5000 (1/mask-time) bytes (total 33 MB) of waveform data per second in FIFO (first-in first-out) mode.

The waveform data was transferred and stored on a personal computer so as to free up memory for subsequent recordings without influencing the waveform recording process, providing virtually unlimited recording capacity. As the transfer of data from the waveform recorder to the computer including hypocenter determination and disk access, took about 0.3 s for each event, real-time hypocenter monitoring was possible only when the AE rate was lower than 3 events/s. At higher rates, the hypocenters were determined with a time delay dependent on the amount of data accumulated in the memory of the waveform recorder.

The velocities along multiple paths were measured using an 18-channel fast-switching system to switch the selected sensor from receiver to detonator and connect the sensor to a pulse generator. Switching all 18 selected sensors one by one took about 1 s. After the experiment, the data obtained using this system allowed the precise velocity structure in the test sample to be reconstructed at each measuring time by travel–time tomography.

Since there is no major loss of AE events even for an event rate of the order of several thousand events per second, it is possible to map out the spontaneous acceleration from quasi-static to dynamic rupture of a fault under constant stress (creep) or constant stress-rate loading conditions by monitoring the detailed spatio-temporal distribution of AE events. This is a more advanced way to study the non-linear faulting process than the method employed in previous studies, which involved stabilization of the failure process through control of the axial stress in order to maintain a low constant rate of AE occurrence (e.g. Lockner et al., 1991). Although constant strain-rate loading has been used in many experimental studies, constant stress loading is also a meaningful loading method for simulating the tectonic forces and conditions in many artificial applications such as tunnels and mines.

2.2. Preliminary data analysis

The main data used in this study includes (1) event rates calculated from the maximum amplitude data, (2) seismic *b*-values for the magnitude–frequency relationship as calculated from the maximum amplitude data, (3) hypocenters determined using the first arrival times at the 32 receivers, (4) the fractal dimension of the hypocenter distribution, and (5) the self-excitation strength for AE occurrence. As a trigger threshold higher than the maximum amplitude recording was employed for waveform recording, the hypocenter data is a subset of the maximum amplitude data. The maximum amplitudes are used to calculate a relative magnitude that is comparable with seismic magnitude for small earthquakes. The noise level after

pre-amplification with a gain of 20 dB was less than 45 dB, providing an effective dynamic range of more than 55 dB, which corresponds to a relative magnitude range of about 2.75. The *b*-values are calculated from the relative magnitude data using the maximum likelihood method (Aki, 1965; Utsu, 1965) for a running window of 500 events and a step of 125 events. The standard error is estimated to be between 0.03 and 0.08 for a *b*-value between 0.5 and 1.5. The path attenuation, which is not considered in the calculation of *b*-values, appears to have no statistically significant effect on the *b*-values, and the maximum amplitude data recorded by two sensors mounted at opposite positions on the cylinder surface of the sample give similar results. Hypocenters were re-determined after each test using the measured *P* velocity during the test. The location error is estimated to be less than 2 ~ 3 mm for most events (Lei et al., 1992), as estimated directly from AE hypocenters in the AF sample.

2.3. Fractal analysis

A two-point correlation integral was applied to examine the spatial clustering of the hypocenters of AE events. The two-point correlation is defined as follows (e.g. Hirata, 1987; Lei et al., 1992).

$$C(r) = \frac{2N_r(R < r)}{N(N-1)} \tag{1}$$

where $N_r(R < r)$ is the number of hypocenter pairs separated by less than r, and N is the total number of AE events analyzed. If the hypocenter distribution is self-similar, $C(r)$ is proportional to r^D, where D is the fractal dimension determined by a least-squares fit of a log–log plot. If a set of hypocenters in a three-dimensional volume is fractal, the fractal dimension will be between 0 and 3.0. Here, $D = 0$ indicates that all hypocenters fall within a discrete volume, while $D = 3.0$ represents the distribution of hypocenters throughout the volume without areas of concentration. Smaller values therefore reflect higher degrees of clustering, and a value itself can represent many patterns of distribution. For example, $D = 2.0$ may represent both a planar distribution and a volumetric distribution with clustering. Similarly, $D = 1.0$ may represent a linear distribution or a volumetric distribution with strong clustering. Hence, the D value must be considered with respect to the general nature of the hypocenter distribution.

2.4. Self-excitation model of AE occurrence

It has been found that AE events do not occur randomly, but rather have a time-dependent probability distribution (Nishizawa and Noro, 1990; Lei et al., 2000c). Lei et al. (2000c) observed that in most cases, the following conditional function models the instantaneous probability of AE occurrence in a short interval:

$$\lambda(t) = \mu_0 + p_1 t + \sum_{t_i < t} g(t - t_i) \tag{2}$$

$$g(t) = a_0 e^{-\beta t} \tag{3}$$

where μ_0 is a constant expressing the stationary Poisson process, $p_1 t$ is the trend component, t_i is the timing of the ith event, and $g(t)$ is the impulse response function used to express the effect of excitation of the preceding event on succeeding events. Integrating the impulse function $g(t)$ gives

$$s = \int_0^\infty g(t)\mathrm{d}t = \int_0^\infty a_0 e^{-\beta t}\mathrm{d}t = \frac{a_0}{\beta} \tag{4}$$

which is a value expressing the strength of the effect of excitation associated with the preceding event on succeeding events, or equivalently, the degree of positive feedback in the dynamics. Following Lei et al. (2000c), this integral is called the self-excitation strength. The parameters in the model are determined based on maximum likelihood theory (see Lei et al. (2000c) for details).

3. Results

Fig. 2 shows the differential stress and cumulative number of AE events against the axial strain (shortness) observed near the fractured fault for all tests. The fracture strengths (maximum differential stress) for the SF, HF, AF, and WF samples were 720, 300, 280, and 150 MPa, respectively. The fault in the SF sample was strong, while that in the WF was weak, as expected. Accordingly, the SF sample fractured suddenly with only a small number of AE events prior to dynamic fracture followed by numerous

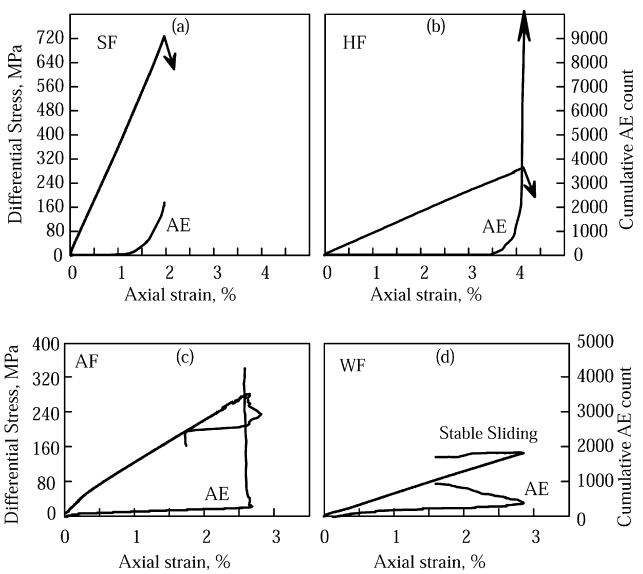

Fig. 2. Differential stress and cumulative AE counts plotted against local axial strain near the fault in the test samples. All samples were loaded at a constant stress rate. Notes that the axial strain is a local measurement.

aftershocks, representing typical brittle fracture behavior (Fig. 2a). The WF sample exhibited ductile rupture behavior with no remarkable AE activity (Fig. 2d). Samples HF and AF have an intermediate fracture strength between that of the SF and WF samples, and exhibited violent AE activity prior to dynamic rupture (Fig. 2b and c). As summarized in Table 1, the AE activity during the fracture process can be grouped into three typical long-term stages according to the time–space statistics of AE events: primary, secondary and nucleation. The term 'pre-nucleation' is also used to refer collectively to the primary and secondary phases. This progression of the fracture process is consistent with the results for an inhomogeneous fault having several mechanical/geometrical asperities presented in the authors' previous paper (Lei et al., 2003). However, new data in this study shows that the statistical characteristics of each stage vary according to the fault type. Event rates, *b*-values and other statistics differ significantly between these phases.

3.1. SF sample

Fig. 3 shows the temporal change in axial strain, differential stress, event rate, *b*-value and self-excitation strength of AEs in the SF sample. The AE activity prior to dynamic rupture is very low, initiating at a stress of ~60% of the peak stress (Fig. 3a). After initiation, the event rate increases slowly with time and stress (Fig. 3b). The *b*-value increases from ~0.75 to 1.0 with increasing stress (Fig. 3c). The secondary phase is characterized by a gradual increase in the event rate and slight decrease in the *b*-value with increasing stress (Fig. 3b and c). The nucleation phase is very short (a few seconds), with only a small number of foreshocks. After the dynamic fracturing, about 2500 aftershocks were observed, accompanied by a high *b*-value of ~1.2. In the primary phase, the self-excitation strength is weak (<0.2), but from the secondary phase to the nucleation phase, this value increases gradually to ~1.0 up to dynamic fracture (Fig. 3d).

Fig. 4 shows an X-ray computed tomography (CT) scan of the sample after the experiment, along with projected hypocenters on planes perpendicular and parallel to the fault plane. In the primary and secondary phases, the AE

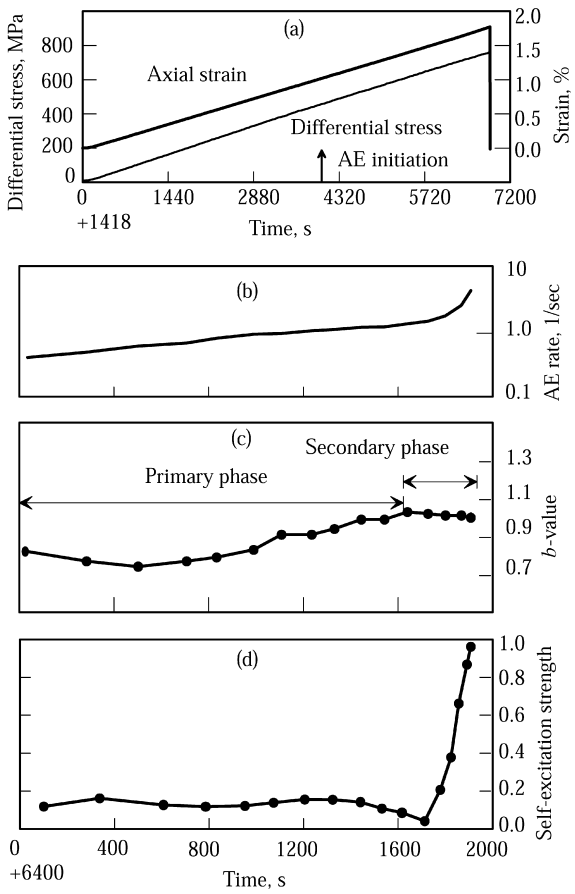

Fig. 3. Basic results for the SF sample: (a) differential stress and axial strain; (b) AE rate; (c) *b*-value; and (d) self-excitation strength after AE initiation. The error bars for the *b*-value are smaller than the symbols in this plot.

hypocenters are distributed throughout the sample volume without remarkable concentration, although some small clusters are apparent. As shown in Fig. 5a, the primary phase has two distinct fractal distributions, with a transition at around 8 mm, which is roughly equivalent to the dominant grain size. The clustering of microcracking therefore appears to be controlled by the spatial distribution of grain size. The long-range fractal dimension D_l (>8 mm) is 2.25, and therefore represents the distribution of clusters in the sample, and the short-range fractal dimension D_s

Table 1
Summary of the main experimental results

Sample	Fracture strength (MPa)	Statistics	Primary phase	Secondary phase	Nucleation phase
SF	720	AE count	~1,500	~540	~200
		b-value	0.8 → 1.05	1.05 → 1.0	
		D	2.25/1.06	1.87	
HF	300	AE count	~500	~1200	~58,000
		b-value	1.1 → 1.3	1.3 → 1.0	1.0 → 0.5
		D	2.00	1.60	1.25/2.25
AF	280	AE count			~4200
		b-value			1.2 → 0.6
		D			1.0
WF	150				

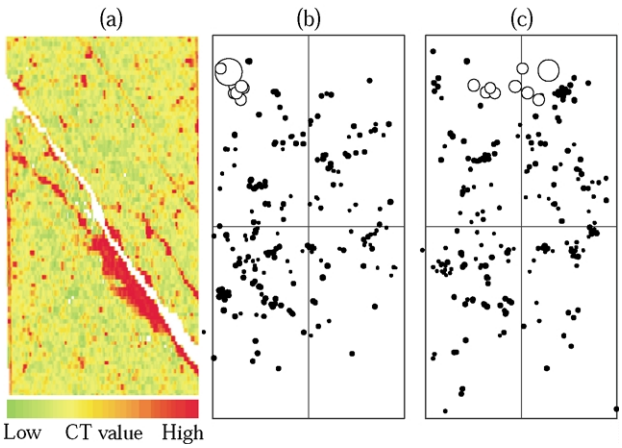

Fig. 4. (a) X-ray CT scan image for the SF sample (the CT value reflects the density of the material matrix). (b) and (c) The AE hypocenters in the SF sample projected to a plane (b) perpendicular and (c) parallel to the rupture plane. Solid circles indicate the events in the pre-nucleation phases; open circles (shown twice as large for clarity) indicate the foreshocks in the nucleation phase.

(<8 mm) is 1.06, reflecting the distribution of hypocenters inside the clusters. This result indicates that the typical size of clusters in the primary phase is about 8 mm. In the secondary phase, D_l decreases to 1.87 while D_s increases to 1.87 (Fig. 5b). Since the nucleation phase included only a few events, it is impossible to calculate the fractal dimension for that phase. However, it can be seen that the foreshocks in the nucleation phase are concentrated at the initiation site on the fault plane (empty circles in Fig. 4b and c). The last (and largest) event produced a very strong waveform, and most likely represents the beginning of dynamic fracture along the pre-existing fault.

3.2. HF sample

Fig. 6 shows the results for the HF sample. This sample clearly demonstrates the three stages of the fracturing process. Fig. 7 is a magnified view of the final 20 s (N3 in Fig. 6b). Large numbers of AE events occurred in all three phases, providing a clear picture of the process. In the primary phase, AE activity initiates at a stress of ~65% of the peak stress, and the event rate increases gradually with time and stress (Fig. 6b). The *b*-value increases slightly

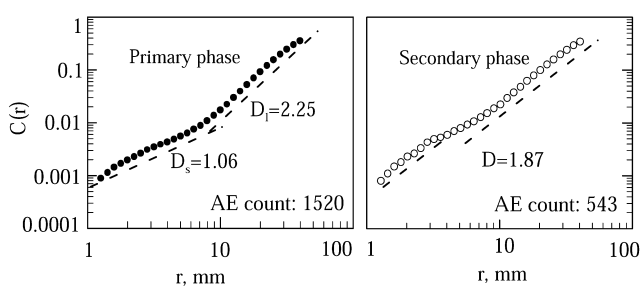

Fig. 5. Correlation integral function for hypocenters in the SF sample against distance using logarithmic coordinates. The fractal dimensions estimated from the slope are also shown.

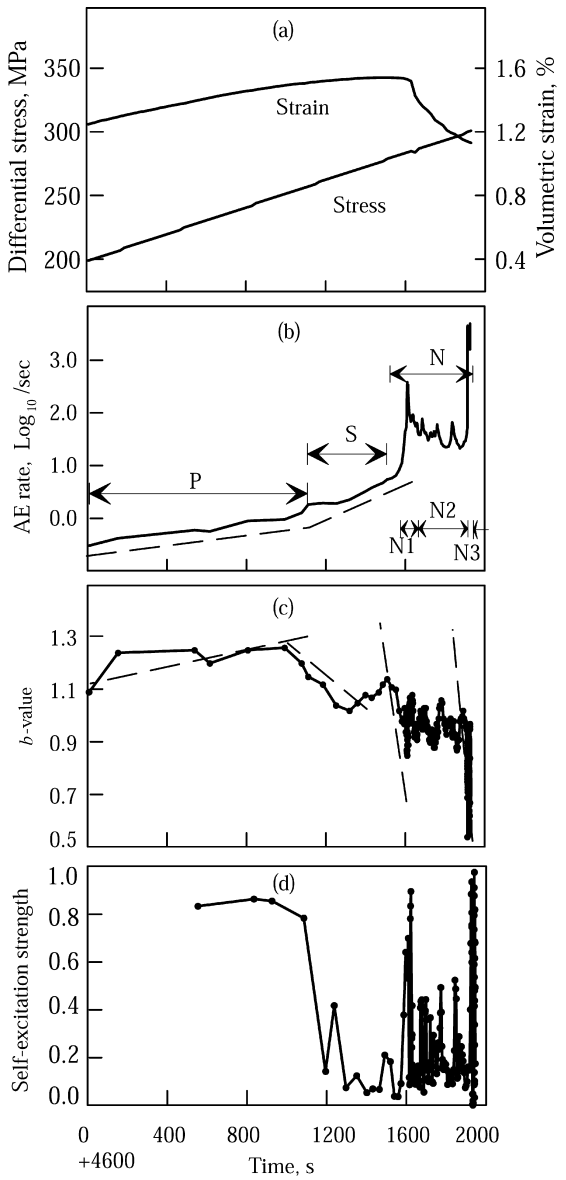

Fig. 6. Basic results for the HF sample: (a) axial stress and volumetric strain against time. Volumetric strain is calculated from the axial and circumferential strains recorded using a cross-type strain gauge near the fracture plane and as such is a local value; (b) logarithmic AE rate against time; (c) *b*-value against time; and (d) self-excitation strength against time. P, S, and N indicate the primary, secondary, and nucleation phases, and the nucleation phase is further divided into sub-phases N1, N2, and N3.

from 1.1 to 1.3, with an average of 1.2 (Fig. 6c). In the secondary phase, the event rate increases with time and stress at a significantly larger slope than the primary phase. The *b*-value decreases with increasing stress from an initial value of ~1.3 to ~1.0 (Fig. 6c). In the nucleation phase, the event rate increases rapidly to 400 AEs/s (N1 in Fig. 6b), followed by a decrease to ~40 AEs/s and fluctuation for about 250 s (N2 in Fig. 6b). Finally, the AE rate increases suddenly to ~5000 AEs/s (N3 in Figs. 6b and 7a), while the *b*-value decreases from ~1.0 to the global minimum of ~0.5 with large fluctuations (Fig. 7b). This nucleation behavior appears to be associated with the particular

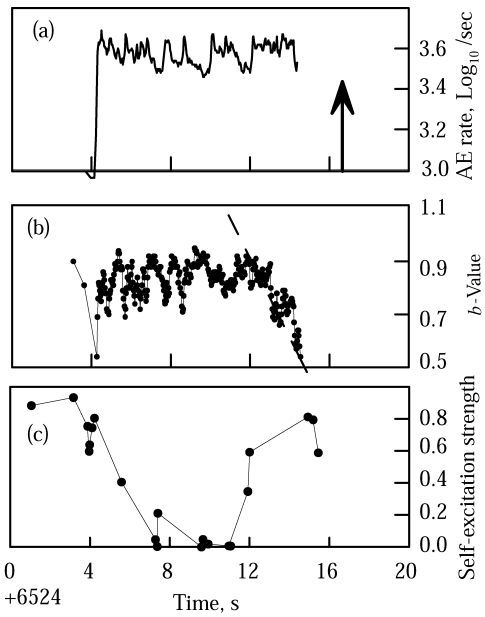

Fig. 7. Detailed view of: (a) the event rate, (b) *b*-value, and (c) self-excitation in the N3 phase shown in Fig. 6. Arrow in (a) indicates the onset of dynamic fracture.

structure of the fault. The fault has an extensional jog at its upper end (Fig. 8a). The first local maximum of the event rate in N1 in fact corresponds to the dense cluster of microcracking around the jog. After the fracture of the extensional jog, the accelerated faulting nucleation process is relaxed due to the sub-critical stress on other unfractured areas of the fault plane.

The average self-excitation strength in the primary phase is 0.8, while that in the secondary phase is less than 0.2, indicating that preceding events tend to trigger successive events in the primary phase, but not in the secondary phase. The nucleation phase is characterized by a highly variable self-excitation strength of 0.5 ~ 1.0. In the N1 (faulting initiation) and N3 (accelerated fault growth) regions in particular, the self-excitation strength reaches the maximum value of ~1.0 (Figs. 6d and 7c).

The most notable feature of the nucleation phase is the short-term contemporaneous fluctuations of the AE rate, *b*-value and self-excitation strength. A local minimum in the *b*-value corresponds to local maxima of both the AE rate and self-excitation strength. After viewing the results of all tests, it is clear that this kind of short-term fluctuation is related to the heterogeneous structure of the fault plane. This will be discussion later in more detail.

The hypocenter distribution in the three phases is shown in Fig. 8, along with a CT image of the sample after the experiment. The hypocenters in the primary phase are distributed throughout the sample volume, with some concentration on a small fault to the lower-left of the main fault (Fig. 8b). The fractal dimension is 2.0 (Fig. 9a), and the correlation integral function has a bend at ~10 mm, indicating a typical cluster size of ~10 mm, which again is equivalent to the predominant grain size of the sample. In the secondary phase, most AEs occur on the pre-existing fault plane (Fig. 8c), and the fractal dimension decreases to 1.6 (Fig. 9b). In the nucleation phase, the hypocenter distribution reveals several dense clusters on the fault plane (Fig. 8e). The long-range and short-range fractal dimension are $D_l = 1.0 \sim 1.38$ and $D_s = 2.25$ (Fig. 9c). These values, and the fact that D_s is much larger than D_l, indicate that clusters are limited to a few sites, but that microcracking events within each cluster fall on the fault plane. The typical cluster size changes between N1, N2 and N3, reflecting the progressive fracture of asperities of different size.

As the main fault ruptured down towards the lower end cap and not to the free surface, the end cap may have affected the nucleation process (N2 to N3). If this is the case, the end cap may have acted as a barrier for shear rupture. Therefore, the longer nucleation process observed for this

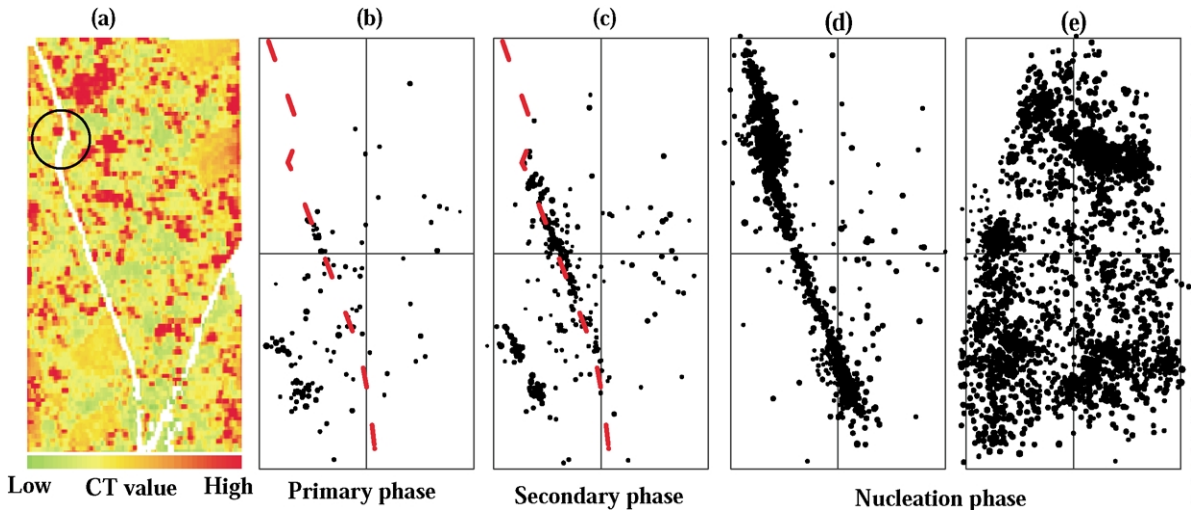

Fig. 8. (a) X-ray CT scan image of the HF sample after the experiment, taken perpendicular to the fault plane. (b)–(d) Plots of AE hypocenters projected onto a plane perpendicular to the fault plane for the (a) primary, (b) secondary and (c) nucleation phases. (e) AE hypocenters in the nucleation phases projected onto a plane parallel to the fault plane.

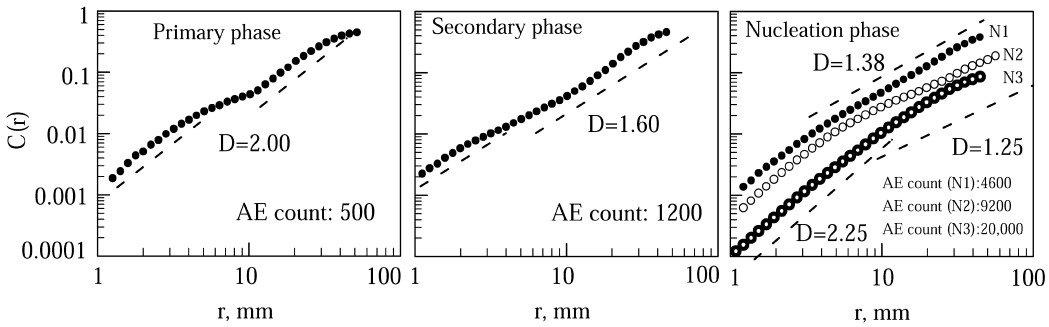

Fig. 9. Correlation integral function for the hypocenters in the HF sample against distance using logarithmic coordinates. The fractal dimensions estimated from the slope are also shown.

sample may be due in part to end effects. However, the progression of the nucleation phase, and fluctuation of the event rate and *b*-value would not be affected appreciably.

3.3. AF and WF samples

Four experiments have been conducted using samples similar to the AF sample, as detailed in previous work (Lei et al., 2000b). Here, the important common results are summarized, and some new analytical results are presented. Figs. 10–13 show the results for one of the AF samples. AEs initiate suddenly and increase rapidly near the peak stress. The *b*-value exhibits fluctuations on a decreasing trend from an initial value of 1.2 ~ 1.4 to a global minimum of 0.5 ~ 0.7 (Fig. 11). As indicated in Fig. 11a, the sample was manually unloaded at the onset of dynamic fracture in order to save the sample from excessive damage. The self-excitation strength before unloading is large (0.5 ~ 1.0). These features of AE activity are similar to the nucleation phase of the SF and HF samples, demonstrating that only the nucleation phase produces high AE activity in AF samples. The primary and secondary phases include only a few weak events, precluding meaningful statistical analysis.

The AE hypocenters are distributed at asperities (intersections of the quartz veins and the fracture plane) where large dilatancy was observed following the rapid increase of AE activity (v2 in Fig. 11a). The hypocenter distribution has a fractal dimension of ~1.0 (Fig. 14), which is consistent with the arrangement of asperities along a line of 1 or 3 mm in width on the fault plane. Hypocenters map out the asperities on the fault plane precisely, allowing a direct estimation of the location error to be made, in this case (<2 ~ 3 mm). Off-asperity segments of the fault exhibit ductile behavior with large compressive deformation but no remarkable AE activity (Lei et al., 2000b). Therefore, fault nucleation appears to be controlled by the asperities of the quartz veins. During loading, stress is concentrated mainly at narrow veins of high strength. The precursory microcracking activity is caused by fracturing of the asperities. Dense microcracking moves from one asperity to another, giving rise to the short-term fluctuations in the *b*-value and event rate. Similar to the HF sample, local maxima of event rate and self-excitation strength, and local minima of *b*-values correspond to dense spatial clusters.

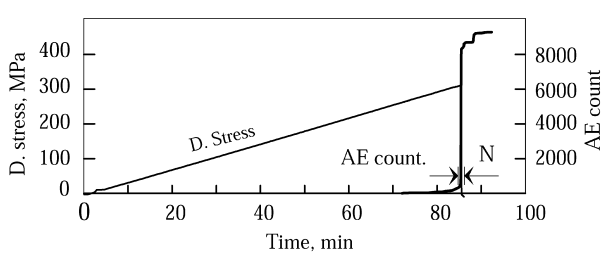

Fig. 10. Experimental results for the AF sample. Differential stress and AE count are plotted against time.

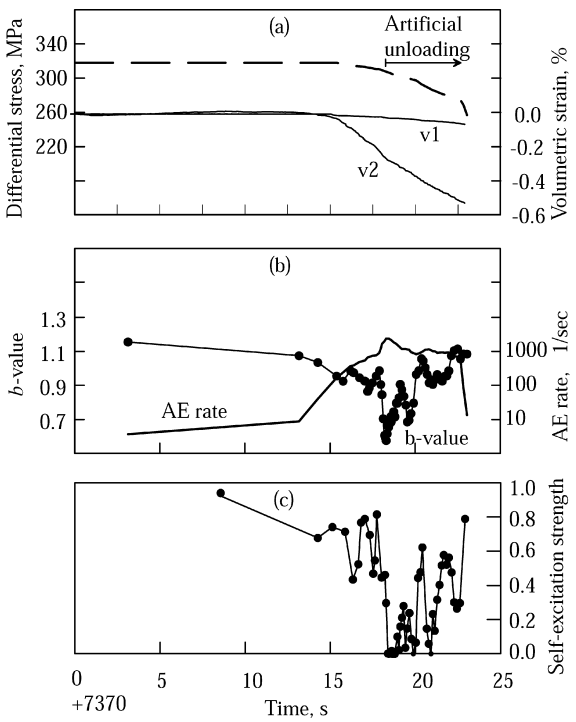

Fig. 11. Detail of the nucleation phase N in Fig. 10. (a) The differential stress and strains at asperities (v2) and off-asperities (v1), (b) logarithmic AE rate and *b*-value, and (c) self-excitation strength are plotted against time. The axial stress was released manually when the dynamic rupture was initiated in order to save the sample from excessive damage.

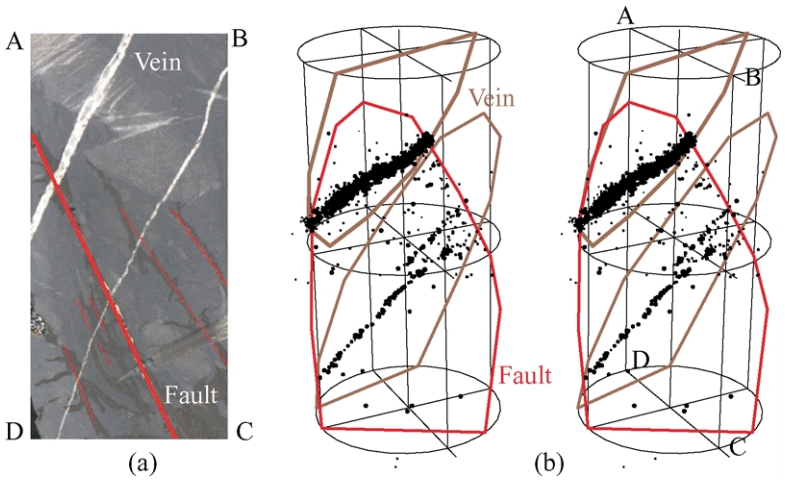

Fig. 12. (a) Photograph of a section of the AF sample after the experiment. (b) Stereo images of all AE hypocenters, showing veins and faults.

The WF sample exhibits a completely different deformation pattern, with a stable or ductile rupture process and very low AE activity (Fig. 2d). Examination of the results for both the AF samples and the WF sample reveals that strong asperities appear to control the nucleation process of rupture. The fracture strength of the WF sample is 150 MPa, while the average for the AF samples is 280 MPa. Although the total area of asperities on the AF fault constitutes only a small fraction of the total fault area, these asperities increase the strength of the fault by 130 MPa, demonstrating that such asperities are very strong and influence the seismic behavior of a fault considerably.

4. Discussion

4.1. Physics behind the three phases of microcracking

AE activities in stressed rock can be theoretically modeled by stress-aided corrosion theory for sub-critical crack growth of a macroscopic crack (e.g. Atkinson, 1984) and a population of microcracks (Meredith et al., 1990; Main et al., 1992, 1993). These models predict a negative relationship between the *b*-value and remote stress, as well as high-order nonlinear crack growth prior to dynamic fracture with a corresponding rapid decrease in the *b*-value. However, in the primary phase, particularly for the SF sample, the *b*-value of AE events exhibits a slightly positive relationship with stress, indicating that earlier microcracking may be governed by some mechanism other than sub-critical crack growth. In fact, in the primary stage, major microcracking could be the result of an initial opening or rupturing of pre-existing microcracks or defects.

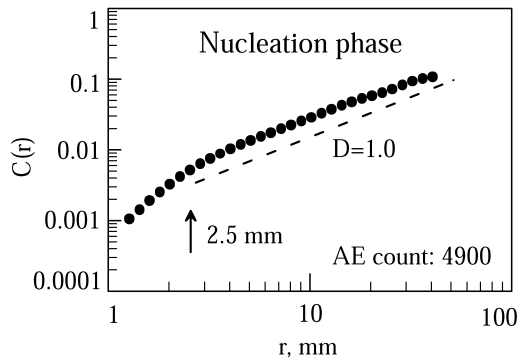

Fig. 13. Correlation integral function for the hypocenters in the AF sample against distance using logarithmic coordinates. The fractal dimensions estimated from the slope are also plotted.

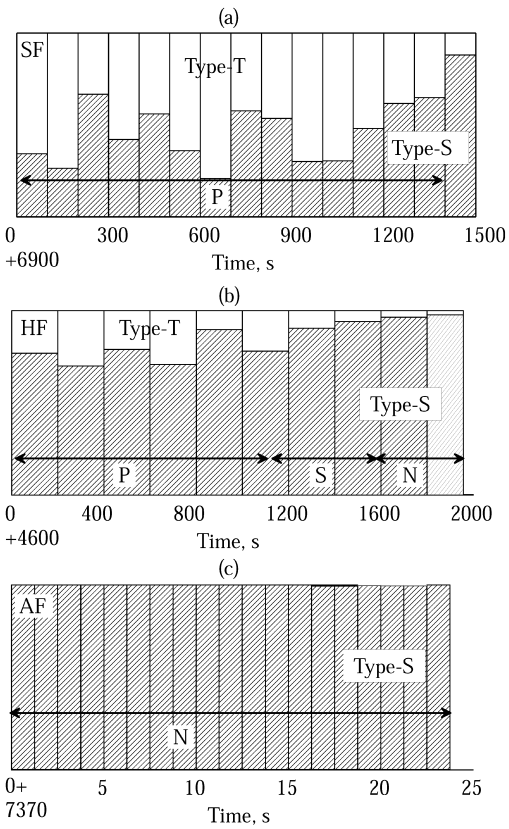

Fig. 14. Cracking mode distribution in the test samples based on the first motion of P-waves. Type-T and Type-S indicate tensile and shear cracking.

Pre-existing microcracks generally heal with a wide range of healing strength, thus separation of the crack walls is more likely to occur than growth of the crack front into unfractured rock. Since extension strength is much lower than shear strength, the opening of pre-existing microcracks can be considered to be an important cracking mode in the primary phase, particularly at relatively low stress.

The cracking mode itself can be determined statistically using the method proposed by Lei et al. (1992). Here, the ratio of up (dilatation) to down (compression) first motions is used to distinguish between tensile cracking (Type T) and shear or shear-dominated cracking (Type S), defined as up/(up + down). To maintain reliability of the data, only data having more than eight reliable first motions were used in this analysis. From a preliminary manual consideration of the ratio, cracking with an up–down ratio larger than 0.75 is considered to be tensile, and all other cracking to be shear or shear-dominated. This analysis revealed that extension cracking is dominant in the primary phase for the SF sample (Fig. 14a). As larger pre-existing microcracks have a higher probability for rupture at lower stress than smaller cracks, this results in a slight increase in *b*-value in primary phase with increasing stress.

The low self-excitation strength in the primary phase for the SF sample is also consistent with this model. In the HF sample, however, the primary phase is characterized by high self-excitation strength. This is probably associated with the earlier fracture of a small sub-fault on the lower side of the main fault, as indicated by the concentration of hypocenters in that region.

In the secondary phase, the event rate increases with stress according to a power law, but with a significantly higher exponent than that of the primary phases. The seismic *b*-value decreases with stress, which is consistent with the sub-critical crack growth model mentioned above. Increasing AE rate, decreasing *b*-values, weak self-excitation strength, and an increase in the predominance of the shear-cracking mode are the important features of the secondary phase. These results indicate that following the increase in crack density and mean crack length, sub-critical crack growth and coalescence of neighboring cracks becomes gradually more important. Therefore, interaction between cracks appears to be a key factor in the secondary phase.

The nucleation stage is the most interesting and important phase in the catastrophic fracture of rock samples with heterogeneous faults. The term ‘nucleation’ is used rather than ‘tertiary’ here for the rapidly increasing microcracking prior to dynamic rupture because this phase corresponds to the nucleation process of the final unstable rupture of the fault in the test sample. In homogeneous brittle rock, the initiated shear fault grows quasi-statically with a process zone at the fault front and is governed by progressive triggering of tensile microcracking, as determined by both microscopic examination (Cox and Scholz, 1988) and AE monitoring (Lei et al., 2000c). The process zone of a shear fault may also include a minor shear microcracking component depending on the material under investigation (Zang et al., 2000).

In rock samples, the pre-existing macroscopic faults are first-order heterogeneities, and the non-uniform healing strength distribution of the fault is a second-order heterogeneity. In the case of a fault with heterogeneous healing strength, AE hypocenters in the nucleation phase do not show a clear fault front, rather, faulting is initiated at several sites in succession in a competing manner, resulting in the observed large amplitude fluctuations in the event rates and *b*-values. Weaker areas and smaller asperities can rupture earlier than stronger areas and larger asperities, and the rupture can be obstructed at the boundary of a strong asperity or barrier, resulting in a short hiatus. Dense microcracking may then occur in the strong asperity when the local stress exceeds the strength of the asperity. A stronger asperity will therefore result in a longer hiatus and consequently higher event rate and lower *b*-value after the hiatus. When an asperity is fractured, aftershocks occur in the asperity area in a relatively lower shear stress environment, resulting in a higher *b*-value. This model reasonably explains the large simultaneous short-term fluctuations in event rate, *b*-value and self-excitation strength observed in the nucleation phase for these samples.

Once the final fault is initiated at one or several key positions, which may be the edges of asperities or fractured areas, the faulting process will be governed by non-linear crack growth, or in other words, the progressive fracture of asperities. Hence, the nucleation phase represents a transition from linear behavior to non-linear behavior. This is considered to be the reason why the change from the secondary phase to the nucleation phase in the experimental results is so abrupt.

The duration of the nucleation phases for the SF, AF, and HF samples are <2, 50, and 300 s (N1: 50 s, N2: 235 s, N3: 15 s), respectively. Although the N2 and N3 periods in the nucleation phase for the HF sample may be affected by the lower cap, the timing of fault nucleation appears to be positively related to the degree of heterogeneity. Highly homogeneous faults such as in the SF sample may exhibit an unpredictable failure style, whereas heterogeneous faults such as that in the HF sample fail in a predictable manner with remarkable precursory anomalies in the statistics of AE activity, indicative of microcracking.

The results of this and previous studies demonstrate that the fracture of fine-grained samples and samples containing faults or joints (Lockner et al., 1991; Satoh et al., 1996; Lei et al., 2003) is characterized by clear localization of hypocenters in the nucleation phase, while this is not commonly observed for intact coarse-grained rock samples with high densities of pre-existing microcracks (Zang et al., 1998; Lei et al., 2000b). In the former case, a thin shear fracture plane initiates and grows, observed as low background activity. In the later case, a wide shear zone forms and grows, with higher background activity. As pre-existing

cracks and mineral grains appear to be the most important factor controlling the local strength of rock, the different nucleation behavior reflects the stress redistribution in a rock sample after the initiation of shear fracture.

4.2. Implication of experimental results

The present experimental results demonstrate that damage creation and catastrophic fracture of faults in rocks is characterized by three typical stages of microcracking. Explicit precursory behaviors were observed in the nucleation phase preceding the dynamic rupture of heterogeneous faults. The microcracking activity can be quantitatively described in terms of the event rate, seismic *b*-value, self-excitation strength, and fractal dimension of the hypocenter distribution. These parameters are closely related to the heterogeneous structure of the fault, such as the distribution of healing strength and asperities. According to the self-similarity of the geological structure, these laboratory-scale experimental results are considered to be basically applicable to larger scales of industrial application and natural earthquakes. Therefore, the statistics of detailed AE or microseismic data can be expected to provide useful parameters for monitoring the status of active faults and identifying potential asperities on a fault plane.

AE data prior to dynamic rupture can be treated as foreshocks (Lei et al., 2003). The present experimental results revealed a precursory *b*-value anomaly: a slight increase and then drop from 1.0 ~ 1.2 to about 0.5. This result is in agreement with the theoretical model of subcritical crack growth (Meredith et al., 1990; Main et al., 1992, 1993), indicating that a decreasing *b*-value reflects stress enhancement due to fracture growth in asperities, and in particular the boundaries of asperities. This long-term tendency is also consistent with that observed before some large earthquakes such as the 1984 Nagano and 1985 Tonga earthquakes (Meredith et al., 1990), the Mw 7.8 Cape Kronotsky, Kamchatka, earthquake on 5 December 1997 (Zuniga and Wyss, 2001), and the Mw 7.9 off-Etorofu (Iturup), Kurile Islands, earthquake on 3 December 1995 (Hurukawa, 1998), as well as volcanic eruptions (Vinciguerra, 1999).

Statistical studies have also shown that variation in the *b*-value of foreshocks is a common feature of natural earthquakes. For example, by comparing *b*-values for long-term seismicity and foreshocks occurring within hours and days prior to a mainshock, Molchan et al. (1999) found that the *b*-value drops by half during the foreshock period. However, this result represents a statistical average, and not the behavior of individual foreshock sequences. Unfortunately, most large natural earthquakes are not preceded by a large number of identifiable foreshocks. To interpret this, two factors must be considered. One is the incompleteness of small earthquake data due to the magnitude threshold for detection. The other is that a well-developed natural fault might be quite homogeneous on small scales, particularly at seismogenic depths, resulting in a low cutoff of magnitude. Clearly, further work is required to evaluate the importance of these factors.

Some studies have found that asperities in the crust can be predicted from the detailed *b*-value distribution calculated from seismic data including earthquakes of magnitude smaller than one (e.g. Wyss et al., 2000). However, it remains difficult to observe all small earthquakes in the upper crust, and it is even more difficult to detect the stress–strain status of a fault at depth. Therefore, experimental approaches such as that adopted in the present study provide an alternative means of clarifying the relationships between fault rupture and fault structure. The validity of rules obtained through experimental studies when applied to seismic activity in the earth also remains an important scientific challenge. To this end, detailed studies on induced microseismicity in mineral fields and dams on an intermediate scale can be expected to provide further data allowing the reliable extension of laboratory results to the analysis of tectonic earthquakes.

5. Conclusion

Through the use of a high-speed multi-channel waveform recording system, the detailed time-space distribution of AE activity was examined during the fracture of four rock samples containing faults of widely differing strength distribution under triaxial compression. The experimental results are generally in agreement with previous data on the fracture of inhomogeneous faults. The AE events were characterized in terms of event rates, seismic *b*-values, the self-excitation strength, and the fractal dimension of the hypocenter distribution. Three long-term microcracking phases: primary, secondary and nucleation, can be identified based on the changes in these parameters. In the primary phase, the AE rate increases gradually with stress, corresponding to early microcracking (mainly tensile mode) during the loading period. In the secondary phase, the event rate increases markedly, indicative of increased interaction between cracks. The nucleation phase appears as a sudden sharp increase in the event rate, and represents the initiation and acceleration of the final rupture. The *b*-values in the three phases also exhibit different trends. In the primary phase, the *b*-value takes an average of ~1.2 and increases slightly with increasing stress. In the secondary phase, the *b*-value starts to decrease slowly, and in the nucleation phase, the *b*-value decreases rapidly. The fractal dimension for scales larger than the typical cluster size, which generally corresponds to the dominant grain size, decreases from ~2.2 in the primary phase to 1.0 ~ 1.4 in the nucleation phase.

In the secondary and nucleation phases, the event rate and *b*-value also exhibit large simultaneous short-term fluctuations. The simultaneous local maximum in the event

rate and local minimum in the *b*-value are considered to represent spatial clustering around an asperity on the rupture fault. These short-term fluctuations in the event rate and *b*-value are characteristic of the heterogeneous healing strength and asperity distribution on the fault plane.

The present experimental results demonstrate that the predictability of catastrophic fault fracture is strongly dependent on the fault heterogeneity. A homogeneously healed fault is notably unpredictable, whereas a fault of non-homogeneous healing strength or asperity distribution undergoes a predictable fracturing process with a remarkably clear nucleation phase that can be observed as a precursory anomaly of the *b*-value or other statistical parameters of AE activity. The appearance of a nucleation phase with decreasing *b*-value, a non-linearly increasing event rate and spatio-temporal clustering can therefore be considered to be a signal of the initiation of catastrophic fracture. This paper focused on the experimental facts; a new constitutive model will be examined as part of future work after more data has been collected.

Acknowledgements

This work was supported by the National Institute of Advanced Industrial Science and Technology of Japan (AIST) and a grant (No. G1998040704) from the Ministry of Science and Technology of China. The authors would like to thank M.V.M.S. Rao and two anonymous referees for helpful comments and suggestions on improvements to the manuscript.

References

Aki, K., 1965. Maximum likelihood estimate of *b* in the formula $\log N = a - bm$ and its confidence. Bulletin Earthquake Research Institute of Tokyo University 43, 237–239.

Atkinson, B.K., 1984. Subcritical crack growth in geological materials. Journal of Geophysical Research 89, 4077–4114.

Cox, S.J.D., Scholz, C.H., 1988. Rupture initiation in shear fracture of rocks: an experimental study. Journal of Geophysical Research 93, 3307–3320.

Hirata, T., 1987. Omori's power law aftershock sequences of microfracturing in rock fracture experiment. Journal of Geophysical Research 92, 6215–6221.

Hurukawa, N., 1998. The 1995 off-Etorofu earthquake: joint relocation of foreshocks, the mainshock, and aftershock and implications for the earthquake nucleation process. Bulletin of Seismological Society of America 88, 1112–1126.

Jouniaux, L., Masuda, K., Lei, X.-L., Nishizawa, O., Kusunose, K., Liu, L., Ma, W., 2001. Comparison of the microfracture localization in granite between fracturation and slip of a pre-existing macroscopic healed joint by acoustic emission measurements. Journal of Geophysical Research 106, 8687–8698.

Lei, X.-L., Nishizawa, O., Kusunose, K., Satoh, T., 1992. Fractal structure of the hypocenter distribution and focal mechanism solutions of AE in two granites of different grain size. Journal of Physics of the Earth 40, 617–634.

Lei, X.-L., Kusunose, K., Nishizawa, O., Cho, A., Satoh, T., 2000a. On the spatio-temporal distribution of acoustic emissions in two granitic rocks under triaxial compression: the role of pre-existing cracks. Geophysical Research Letter 27, 1997–2000.

Lei, X.-L., Nishizawa, O., Kusunose, K., Cho, A., Satoh, T., 2000b. Compressive failure of mudstone samples containing quartz veins using rapid AE monitoring: the role of asperities. Tectonophysics 328, 329–340.

Lei, X.-L., Kusunose, K., Rao, M.V.M.S., Nishizawa, O., Satoh, T., 2000c. Quasi-static fault growth and cracking in homogeneous brittle rock under triaxial compression using acoustic emission monitoring. Journal of Geophysical Research 105, 6127–6139.

Lei, X.-L., Kusunose, K., Satoh, T., Nishizawa, O., 2003. The hierarchical rupture process of a fault: an experimental study. Physics of the Earth and Planetary Interiors 137, 213–228.

Lockner, D.A., Byerlee, J.D., Kuksenko, V., Ponomarev, A., Sidorin, A., 1991. Quasi-static fault growth and shear fracture energy in granite. Nature 350, 39–42.

Main, I.G., Meredith, P.G., Sammonds, P.R., 1992. Temporal variations in seismic event rate and *b*-values from stress corrosion constitutive laws. Tectonophysics 211, 233–246.

Main, I.G., Sammonds, P.R., Meredith, P.G., 1993. Application of a modified Griffith criterion to the evolution of fractal damage during compressional rock failure. Geophysics Journal International 115, 367–380.

Meredith, P.G., Main, I.G., Jones, C., 1990. Temporal variations in seismicity during quasi-static and dynamic rock failure. Tectonophysics 175, 249–268.

Molchan, G.M., Kronrod, T.L., Nekrasova, A.K., 1999. Immediate foreshocks: time variation of the *b*-value. Physics of the Earth and Planetary Interiors 111, 229–240.

Nishizawa, O., Noro, H., 1990. A self-exciting process of acoustic emission occurrence in steady creep of granite under uniaxial stress. Geophysical Research Letter 17, 1521–1524.

Satoh, T., Shivakumar, K., Nishizawa, O., Kusumase, K., 1996. Precursory localization and development of microfracture along the ultimate fracture plane in amphibolite under triaxial creep. Geophysical Research Letters 23, 865–868.

Utsu, T., 1965. A method for determining the value of *b* in a formula $\log N = a - bm$ showing the magnitude–frequency relation for earthquakes (in Japanese). Geophysical Bulletin 13, pp. 99–103, Hokkaido University, Hokkaido, Japan.

Vinciguerra, S., 1999. Seismic scaling exponents as a tool in detecting stress corrosion crack growth leading to the September–October 1989 flank eruption at Mt. Etna volcano. Geophysical Research Letter 26, 3689–3692.

Wyss, M., Schorlemmer, D., Wiemer, S., 2000. Mapping asperities by minima of local recurrence time: San Jacinto–Elsinore fault zones. Journal of Geophysical Research 105, 7829–7844.

Zang, A., Wagner, F.C., Stanchits, S., Dresen, G., Andresen, R., Haidekker, M., 1998. Source analysis of acoustic emissions in Ave granite cores under symmetric and asymmetric compressive loads. Geophysical Journal International 135, 1113–1130.

Zang, A., Wagner, F.C., Stanchits, S., Janssen, C., Dresen, G., 2000. The fracture process zone in granite. Journal of Geophysical Research 105, 23651–23661.

Zhao, Y., 1998. Crack pattern evolution and a fractal damage constitutive model for rock. International Journal of Rock Mechanics and Mining Science 35, 349–366.

Zuniga, F.R., Wyss, M., 2001. Most- and least-likely locations of large to great earthquakes along the Pacific coast of Mexico estimated from local recurrence time based on *b*-values. Bulletin of Seismological Society of America 91, 1717–1728.